Bioactive Materials 11 (2022) 181–191

Contents lists available at ScienceDirect

Bioactive Materials

journal homepage: www.sciencedirect.com/journal/bioactive-materials

Formation of a ZnO nanorods-patterned coating with strong bactericidal capability and quantitative evaluation of the contribution of nanorods-derived puncture and ROS-derived killing

Jing Ye [a,1], Bo Li [a,**,1], Mei Li [a,b], Yufeng Zheng [c], Shuilin Wu [d], Yong Han [a,*]

[a] State Key Laboratory for Mechanical Behavior of Materials, Xi'an Jiaotong University, Xi'an, 710049, China
[b] Department of Orthopedics, Guangdong Provincial People's Hospital, Guangdong Academy of Medical Sciences, Guangzhou, 510080, China
[c] Center for Biomedical Materials and Tissue Engineering, Academy for Advanced Interdisciplinary Studies, Peking University, Beijing, 100871, China
[d] School of Materials Science & Engineering, The Key Laboratory of Advanced Ceramics and Machining Technology By the Ministry of Education of China, Tianjin University, Tianjin, 300072, China

ARTICLE INFO

Keywords:
Anti-bacteria
ZnO nanorods
Hydrothermal treatment
Formation mechanism
Bactericidal contributors quantitation

ABSTRACT

To endow Ti-based orthopedic implants with strong bactericidal activity, a ZnO nanorods-patterned coating (namely ZNR) was fabricated on Ti utilizing a catalyst- and template-free method of micro-arc oxidation (MAO) and hydrothermal treatment (HT). The coating comprises an outer layer of ZnO nanorods and a partially crystallized inner layer with nanocrystalline TiO_2 and Zn_2TiO_4 embedded amorphous matrix containing Ti, O and Zn. During HT, Zn^{2+} ions contained in amorphous matrix of the as-MAOed layer migrate to surface and react with OH^- in hydrothermal solution to form ZnO nuclei growing in length at expense of the migrated Zn^{2+}. ZNR exhibits intense bactericidal activity against the adhered and planktonic *S. aureus in vitro* and *in vivo*. The crucial contributors to kill the adhered bacteria are ZnO nanorods derived mechano-penetration and released reactive oxygen species (ROS). Within 30 min of *S. aureus* incubation, ROS is the predominant bactericidal contributor with quantitative contribution value of ~20%, which transforms into mechano-penetration with prolonging time to reach quantitative contribution value of ~96% at 24 h. In addition, the bactericidal contributor against the planktonic bacteria of ZNR is relied on the released Zn^{2+}. This work discloses an in-depth bactericidal mechanism of ZnO nanorods.

1. Introduction

Titanium (Ti)-based endosseous implants are clinically used for repair of bone fracture, due to their good mechanical property, corrosion resistance and biocompatibility. However, implant-associated infection caused by bacteria, especially by *Staphylococcus aureus* (*S. aureus*) seriously impairs osseointegration and extremely shortens life-span of Ti-based implants [1–3].

To endow Ti-based orthopedics implants with bactericidal capability, surface modification coatings containing antibiotics, antibacterial organic (such as macromolecules, peptides), and inorganic components (such as Ag^+, Cu^{2+}, CuO and ZnO) were immobilized on Ti substrates [4]. Compared to the antibiotics and organic bactericide, inorganic bactericidal substance exhibits strong broad-spectrum antibacterial activities without inducing bacterial resistance [5]. Therein, nano-structured ZnO have been widely investigated, including the fields of anti-bacteria [4], fluorescence emission [6], photocatalysis [7] and photoelectrocatalysis [8,9]. More importantly, nano-sized ZnO exhibits negligible toxicity towards mammalian cells according to Federal Drug Administration (FDA) [10], but displays bactericidal capability. In addition, bactericidal activity of ZnO does not rely on other physical stimulation, such as photo- and/or sono-irradiation [11]. Notably, the bactericidal activity of nano-structured ZnO dependents on geometric morphologies, and nanorod-shaped ZnO shows higher bactericidal activity than nanodisk- and nanosphere-shaped ZnO [12,13]. Therefore, it is indicated the great potential of constructing ZnO nanorods-arrayed

Peer review under responsibility of KeAi Communications Co., Ltd.
* Corresponding author.
** Corresponding author.
E-mail addresses: libo1137@xjtu.edu.cn (B. Li), yonghan@mail.xjtu.edu.cn (Y. Han).
[1] Co-first authors: These authors contributed equally to this work.

https://doi.org/10.1016/j.bioactmat.2021.09.019
Received 17 July 2021; Received in revised form 21 August 2021; Accepted 7 September 2021
Available online 16 September 2021

coating (ZNR) on Ti to realize bactericidal function against *S. aureus*.

For constructing ZNR, many methods have been tried in previous works, but these methods exhibit limitations. For instance, vapor-liquid-solid transition and thermal chemical vapor deposition (TCVD) require high temperature (>950 °C) to form ZnO nanorods during these processes, giving rise to formation of thermal stress in the coatings to weaken its adhesion strength [11]; when pulsed laser deposition (PLD) is employed to grow ZnO nanorods, the underlying substrates are required to have a small lattice mismatch relative to ZnO [14]. In addition, catalysts are usually needed during CVD and PLD for preparing ZnO nanorods [15,16], leading to the relatively high cost and risk of biosafety. Hydrothermal treatment (HT) can also be employed to synthesize ZnO nanorods at relatively low temperature (<200 °C) without additional of catalysts, while structure-directing template and ZnO seeds are needed during HT processes [17], and hydrothermally grown ZnO nanorods from the as-prepared ZnO seeds always exhibit weak adhesion to their underlying substrates [18]. Alternatively, it has been reported that nanoplate-like ZnO can be formed on micro-arc oxidized (MAOed) TiO_2 coating at 200 °C in Zn^{2+} contained alkaline aqueous solution using HT without catalysts, template and ZnO seeds [19]. More importantly, micro-arc oxidation (MAO) and HT derived nanorods-patterned arrays composed of inorganic components, such as hydroxyapatite, exhibit firm adhesion to its underlying MAOed matrix, ascribing to the embedded roots of the nanorods into the matrix [20–22]. Although MAO and HT show great superiority in preparing nanorods-patterned arrays, fabrication of ZNR on Ti-based substrates by means of MAO and HT has not been explored yet.

More crucially, although current works have already identified the bactericidal effects of ZNR against *S. aureus*, the underling bactericidal mechanisms of ZNR also have not been elucidated [23,24]. Recently, three kinds of possible bactericidal mechanisms of rod-like ZnO nanoparticles were disclosed: (1) ZnO rod-like nanoparticles tend to puncture bacterial cell membrane during direct nanoparticle/bacteria contact [11,25]; (2) reactive oxygen species (ROS, including $\bullet O^{2-}$, H_2O_2, and $\bullet OH$) derived by the Zn–O bond contained in ZnO rod-like nanoparticles destroy cell membranes and deactivate cellular surface proteins to induce cell death [11]; (3) Zn^{2+} released from the rod-like nanoparticles penetrates into bacterial cytoplasm to induce oxidative stress [26], leading to the inhibition of enzymes function and inactive of proteins and DNA [27,28]. However, regarding to ZNR, in spite of the speculation that physical puncture, ROS formation, and Zn^{2+} release possibly play important roles in killing *S. aureus*, but there lacks of sufficient experimental evidence [23,24]. It is further noteworthy that among the aforementioned contributors, quantitative contribution of each contributor to the synthetical bactericidal activity of ZNR has not been investigated, and their variation trend with incubation time of *S. aureus* on ZNR is also needed to be illuminated.

In the present work, a ZNR with firm adhesion to Ti-based substrate was fabricated by means of MAO and HT, as schematically illustrated in Fig. 1. The hydrothermal grown mechanism of ZnO nanorods was detailedly investigated, and the bactericidal activity against *S. aureus* of the coating was characterized *in vitro* and in rat bone shaft. Especially, at different time points of *S. aureus* cultured on ZNR, quantitatively evaluated contribution of physical puncture, ROS and released Zn^{2+} to the bactericidal activity of ZNR were elucidated.

2. Materials and experimental methods

2.1. Microarc oxidation and hydrothermal treatment

φ 14 × 2 mm and φ 1.4 × 4 mm sized commercial pure Ti discs and pillars were respectively applied as substrates for micro-arc oxidation (MAO), using a home-made pulse power supply (Xi'an Jiaotong University, China). The detailed process was described in our previous work [26]. Briefly, the Ti discs or pillars were ground, washed and used as anodes, the stainless steel plates were used cathodes. Thereafter, the discs and pillars were received MAO one by one in 0.2 M zinc acetate contained aqueous electrolyte at 530 V applied voltages, 100 Hz pulse frequency and 26% duty ratio for 1 min. The obtained coating was termed as MAO_0, and the coating coated Ti was named as M-Ti.

For the hydrothermal treatment (HT), each of the M − Ti discs or pillars was put into a 60 mL volumetric Teflon-lined autoclave, followed by adding 10 mL aqueous solution containing 0.01 M NaOH into the autoclave to immerse the M-Ti. Subsequently, the sample contained autoclave underwent HT at 140 °C for 1, 2, and 4 h. The hydrothermally treated (HTed) MAO_0 were overall referred as HT coatings. The obtained coating which HT for 4 h was termed as ZNR, and the coating coated Ti discs and pillars, namely ZNR-Ti, were cleaned with deionized water and dried in an oven overnight at 60 °C.

2.2. Al–O contained layers deposition on each ZnO nanorods using ALD

An ALD equipment (F-100-41, MNT Micro and Nanotech Co., LTD, China) was used to coat Aluminum (Al) and Oxygen (O) (Al–O) contained layers on ZnO nanorods. Trimethylaluminum and 40 vol% hydrogen peroxide (H_2O_2) aqueous solution were used as precursors of Al and O, respectively, and high-purity N_2 was used as the purged gas. The ZNR-Ti discs were put into chamber of the ALD equipment, followed by vacuating the chamber to 10^{-3} Pa and heating the chamber up to 150 °C. Subsequently, Al and O precursors and N_2 were sequentially auto-injected into the chamber following the sequence of 1 s TMA expose/20 s N_2 purge/0.2 s H_2O_2 expose/40 s N_2 purge for each deposition cycle. After 200 deposition cycles, Al–O coated ZNR-Ti were obtained and termed as Al–O@ZNR-Ti.

2.3. Structure analyses of the coatings on Ti discs

Phases identifications of MAO_0 and HT coatings were carried out by X-ray diffractometer (X'Pert PRO, Netherland) in θ-2θ geometry using Cu-Kα (λ = 0.15406 nm) radiation over 2θ angles of 20–60° at a step of 0.02° with 40 kV scanning voltage and 40 mA scanning current, and the phases obtained from the XRD spectra were identified by the ICDD cards. A field emission scanning electron microscope (FE-SEM; FEI QUANTA 600F, U.S.A.) equipped with an energy-dispersive X-ray spectrometer (EDX) was used for examining the morphologies and elemental compositions of the coatings. Transmission electron microscopy (TEM; JEM-

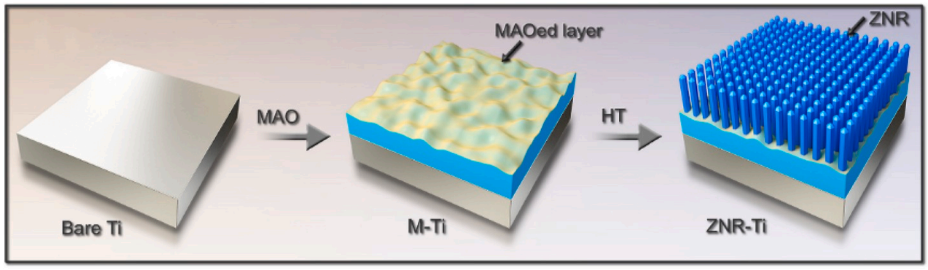

Fig. 1. Schematic illustration of the fabrication process for the ZNR-patterned coating on Ti.

2100F, JEOL, Japan) operating at 200 kV was employed to observe the cross-sectional structure of the coatings and individual nanorod. In addition, the exact elemental compositions within nanoscale regions of the coating cross-section were analyzed using EDX with an approximate 1 nm-diametric electron beam spot under STEM mode equipped in the TEM [29].

2.4. Evaluation of bond strengths and Zn^{2+} release of the coatings on Ti discs

Scratch tests were carried out to identify the bond strength of ZNR on Ti discs utilizing an auto scratch coating tester, which consists of a spherical diamond indenter sliding at a constant speed across a coating surface under various loads to generate a scratch. The critical load, L_c, was defined as the smallest load at which a recognizable failure occurred, and was determined from the curve of acoustic output versus load. Three coated discs were tested and the obtained L_c were averaged.

Immersion tests were used to evaluate the Zn^{2+} release from the coatings. Briefly, the coated Ti discs were immersed in 50 ml PS solutions (i.e., 0.9 wt% NaCl aqueous solutions) at 37 °C for 1, 3, 7, 14, 21, 30, 45 and 60 days, respectively and six samples were used at each time point for each kind of the coated discs. Zn^{2+} concentration of each coated disc immersed solution was examined by an inductively coupled plasma atomic emission spectrometry (ICP-AES; PerkinElmer, Optima 3000 Dv, U.S.A.), and the obtained values were averaged.

2.5. Analysis of extracellular reactive oxide species (ROS) formation

Superoxide ($O_2^{-}\cdot$) and hydroxyl radical (HO·) formed in the bare Ti, ZNR-Ti and Al–O@ZNR-Ti discs immersed Mueller Hinton broth (MHB), which was used to culture bacteria, were examined by electron spin-resonance (ESR) spectroscopy (EMXplus, Bruker, Germany). As described in other work [30], 2, 2, 2, 6, 6-tetramethylpiperidine (TEMP, 39.5 mM; Labotec, Tokyo, Japan), and 5, 5-dimethy-1-pyrolline-*N*-oxide (DMPO, 8.80 mM; Labotec, Tokyo, Japan) were used as spin traps for $O_2^{-}\cdot$ and HO·, respectively. Briefly, the bare and coated Ti discs were placed centrally in 24-well tissue culture plates (TCP), each well was added 500 μL MHB to immerse the disc for 20 s, followed by pipetting 24 μL of the MHB to mix with 1 μL TEMP or DMPO. The mixture was transferred to a quartz tube for ESR measurements.

The hydrogen peroxide (H_2O_2) assay kits (Beyotime Biotech, China) were used to detect the H_2O_2 concentrations in the bare Ti, ZNR-Ti and Al–O@ZNR-Ti discs immersed MHB. Briefly, each disc was immersed in 500 μL MHB for 20 min, and then 50 μL of the MHB was pipetted to mix with 100 μL chromogenic regents in the assay kits. After 30 min of incubation at room temperature, the absorbance value of the mixture was measured at 560 nm, and the concentrations of H_2O_2 in the MHB were drawn from a standard curve of absorbance versus known standards of H_2O_2 concentrations run in parallel with the experimental mixture. All the above mentioned tests were independently repeated three times.

2.6. In vitro antibacterial assays

2.6.1. Antibacterial activities of ZNR-Ti

In the antibacterial tests *in vitro*, Gram-positive bacteria, *Staphylococcus aureus* (*S. aureus*, ATCC 25293) and gram-negative bacteria, *Escherichia coli* (*E.coli*, ATCC25922) were used as model bacteria, which were inoculated twice to obtain bacteria in the mid-logarithmic phase of growth for the tests. For the plate-counting tests, the sterilized bare Ti, ZNR-Ti and Al–O@ZNR-Ti discs were placed in 24-well TCP, 1 mL bacterial suspension (i.e., 1×10^5 CFU bacteria contained MHB) was added into each well to incubate for 24 h at 37 °C. Then, the planktonic viable bacteria in the obtained suspensions were counted using the National Standard of China GB/T 4789.2 protocol. Meanwhile, the aforementioned bare Ti, ZNR-Ti and Al–O@ZNR-Ti cultured with bacteria suspension were rinsed with phosphate-buffered solution (PBS), followed by 5 min of ultrasonic vibration in 1 mL PBS for detaching the bacteria adhered on the discs [31], and the resultant bacterial suspensions were used to count the viable bacteria according to GB/T 4789.2 protocol. Each test was repeated four times.

Live/Dead Baclight Bacterial Viability Kits (Thermofisher, U.S.A.) were employed for detecting the viable bacteria adhered on the bare Ti and ZNR-Ti discs. After incubation for 24 h, each bacteria-adhered disc was rinsed three times with PBS, and then 500 μL PBS containing 10 μM SYTO 9 and 60 μM propidium iodide dyes was added to each well and incubated at 37 °C for 15 min. After fluorescence staining, the images of the stained bacteria were captured by a laser confocal microscope (FV1200, Olympus, U.S.A.).

To observe the morphologies of bacteria cultured on the bare Ti and ZNR-Ti discs, after 24 h of incubation in the bacterial suspension, the bacteria-adhered discs were rinsed with PBS, fixed in 2.5% glutaraldehyde at 4 °C for 1 h, dehydrated in ethanol, dried, and coated with platinum prior to morphology observation by FE-SEM (FEI QUANTA 600F, U.S.A.).

The microscopic interface structures between *S. aureus* and ZnO nanorods were analyzed *via* TEM. The ZNR-Ti disc subjected to bacteria incubation for 4 h was ultrasonically vibrated in PBS to detach the seeded bacteria together with the underlying ZnO nanorods. The resultant suspension was centrifuged to collect the precipitate, followed by fixing with 2.5% glutaraldehyde at 4 °C for 1 h. The obtained precipitation pellet was washed twice with PBS and dehydrated with graded ethanol prior to embedding in Procure 812 resin, and then the embedded resin was cut into ultrathin slices with a thickness of about 100 nm for Bio-TEM (Philips EM 201, U. S. A.) observation.

In parallel, the structural integrities of the *S. aureus* cultured on the bare and ZNR-Ti discs were tested by the protein leakage assay. As described in previous work [26], *S. aureus* were incubated on bare Ti and ZNR-Ti discs for 3, 12 and 24 h. At each time point, the MHB culturing bacteria seeded on the discs were collected and centrifuged to get the supernatant, followed by detecting the total amounts of protein contained in the obtained supernatant using BCA protein assay kit (Thermofisher, U. S. A.) in the light of the manufacturer's instruction. In this experiment, blank MHB, MHB culturing bacteria seeded on TCP and 0.1 M H_2O_2 contained MHB culturing bacteria seeded on TCP were used as control groups.

2.6.2. Analyses of intracellular ROS of S. aureus cultured on the bare and ZNR-Ti discs

Intracellular ROS of *S. aureus* cultured on the bare Ti and ZNR-Ti discs were tested using intracellular ROS assay kits (Beyotime). After 4 h of incubation, the bacteria-seeded discs were rinsed with PBS twice. 500 μL PBS containing 10 μM 2′,7′-dichloroflorofluorescin diacetate (DCFH-DA) was added to each well for loading the fluorescence probe into the bacteria, followed by incubating at 37 °C for 30 min in darkness. The fluorescence stained bacteria were observed by the laser confocal microscope (FV1200, Olympus). In the test, *S. aureus* cultured on bare Ti in 0.1 mM H_2O_2 contained MHB was used as positive control.

2.7. Anti-bacterial capability of the ZNR-Ti pillar in vivo

2.7.1. Implantation of the bare and ZNR-Ti pillars in bacteria infected tibias of rats

Sprague-Dawley rats with average 200 g weight were used for the following *in vivo* experiments, which were approved by the Institutional Animal Care and Use Committee (IACUC) of Xi'an Jiaotong University. 4% chloral hydrate was intraperitoneally injected by weight-adopted (0.3 mL/100g) to anesthetize the rats. For each rat, both lower limbs were shaved and disinfected with povidone iodine, followed by making a 5 mm skin incision at each of the tibial diaphyses to drill a φ 1.5 mm hole on each diaphysis. Subsequently, 20 μL *S. aureus* suspensions with the concentration of 1×10^6 CFU mL^{-1} were injected into the holes using a microsyringe prior to the φ 1.4 × 4 mm sized bare Ti or ZNR-Ti

pillars being parallelly inserted into the marrow cavity from the pre-drilled hole, and then the muscle, subcutaneous tissue, and skin were sutured. After surgery, the rats were housed in separate cages and allowed to move freely. No antibiotic was administered.

2.7.2. Radiographic evaluation

After 4 weeks of implantation, lateral radiographs of the tibias containing the bare Ti and ZNR-Ti pillars were taken using radiographic meter (ALOKA, Hitachi, Japan).

2.7.3. Microbiological examination

The rats were sacrificed after 4 weeks post-surgery, and the explanted bare Ti and ZNR-Ti pillars and pulverized peri-implant bone were rolled over on blood agar plates, which were incubated for 24 h at 37 °C to quantify the viable bacteria adhered on the bare Ti and ZNR-Ti pillars as well as peri-implant bone by means of the GB/T 4789.2 protocol. For each kind of the pillars, six samples were repeated in the experiment.

2.8. Statistical analysis

The data were expressed as mean ± standard deviation (SD) from repeated independent experiments. The data were analyzed using SPSS 16.0 software (SPSS, U.S.A.). One-way ANOVA followed by a least-significant-difference (LSD) post hoc test was used to determine the level of significance. Here, $p < 0.05$ and 0.01 were considered to be

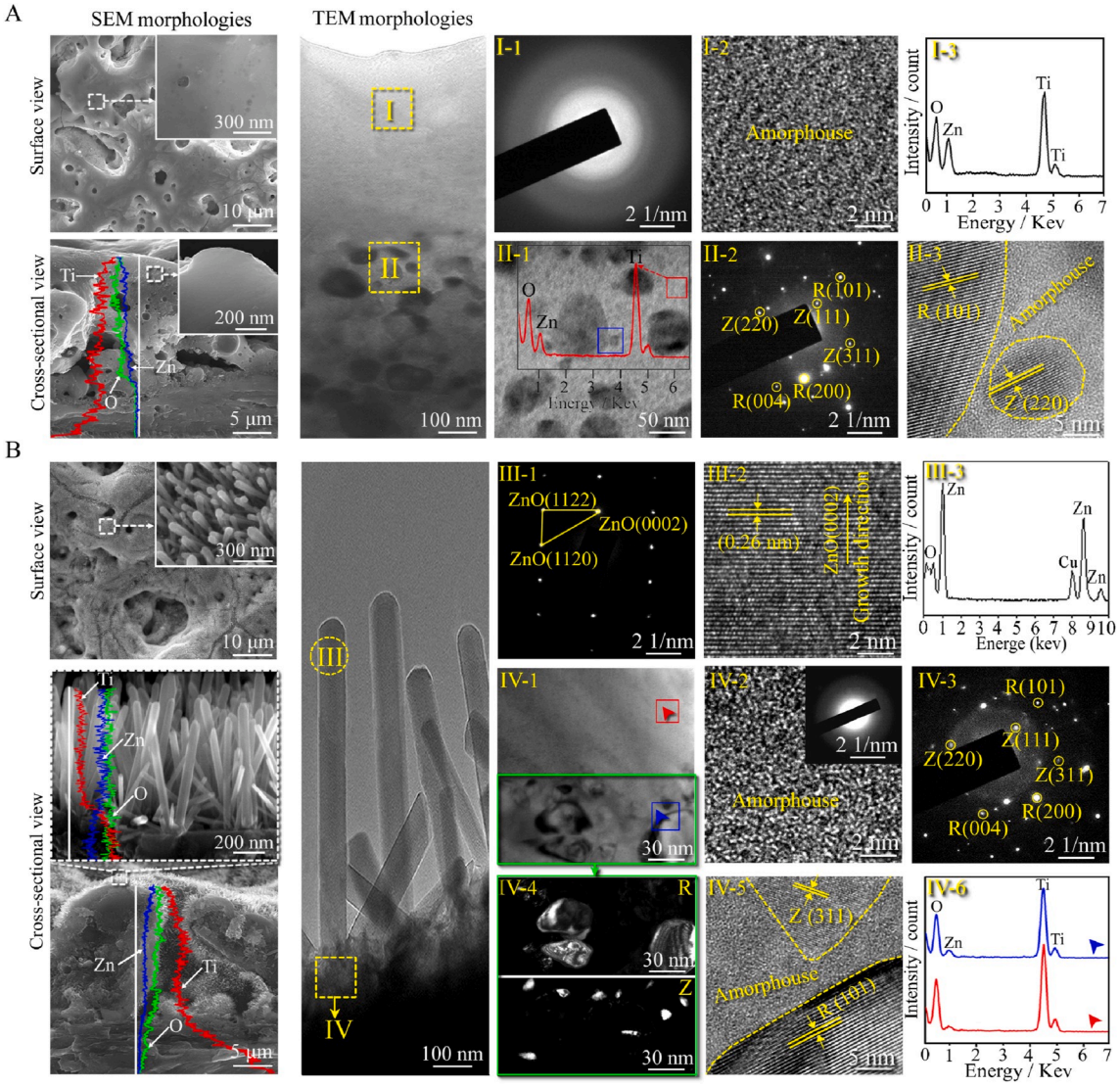

Fig. 2. Microstructures of MAO_0 and ZNR. (A) SEM morphologies and TEM analyzed cross-sectional structure of MAO_0: the panoramic bright field image depicted cross-sectional morphological outline of MAO_0, for the detailed structure of I-marked surface layer in the panoramic bright-field image, I-1, I-2 and I-3 showing the corresponding SAED pattern along with the HRTEM image and EDX spectrum, respectively; taken from II-marked underlying layer in the panoramic bright-field image, II-1 and II-2 showing the magnified image (the inset showing the EDX spectrum detected with the red line square-marked region) and SAED pattern, II-3 showing the HRTEM image of the blue dotted-square marked region in II-1, respectively; (B) SEM surface and cross-sectional morphologies, along with EDX profiles as well as TEM analyzed cross-sectional structure of ZNR: the panoramic bright field image depicted cross-sectional morphological outline of ZNR, for the detailed structure of III-marked an individual nanorod in the panoramic bright-field image, III-1, III-2 and III-3 showing the corresponding SAED pattern along with the HRTEM image and EDX spectrum, respectively; taken from IV-marked underlying layer in the panoramic bright-field image, IV-1 showing the magnified image, and IV-2 showing the HRTEM image of the red line square-marked region in IV-1 (the inset showing the corresponding SAED pattern), IV-3 showing the SAED pattern of the green line square-marked region in IV-1, and IV-4 showing the dark-field image corresponding to R (110) together with Z (311) in IV-3, IV-5 showing the HRTEM image of the blue line square-marked region in IV-1, IV-5 showing the EDX spectrum detected with the red and blue arrows-marked region in IV-1, respectively. The abbreviations R and Z denote Rutile and Zn_2TiO_4, respectively.

significant and highly significant, respectively.

3. Results and discussion

3.1. Microstructures of the as-MAOed coating and hydrothermally grown nanorods-patterned array

MAO_0 reveals a micro-porous topography with 2–15 μm diametric micropores uniformly distributed on the surface. MAO_0 has a uniform thickness of ~20 μm, as identified by the EDX profiles of Ti, O, and Zn detected on the cross-section of the coating. From the surface and cross-sectional views, the micropores' walls and the outmost part of the coating matrix show a smooth and quite dense structure (left image in Fig. 2A), comprising rutile TiO_2 (r-TiO_2) and Zn_2TiO_4 as identified by XRD spectrum in Fig. S1 (Supplementary data). The hyperfine structure of MAO_0 was carefully examined using TEM (right image in Fig. 2A). Obviously, two layers with different crystallinity are contained in the coating. I-marked upper-layer with thickness of ~500 nm consists of complete amorphism (Fig. 2A–I1 and I2) and contains elements of Ti, O and Zn (Fig. 2a–I3), while the II-marked sub-layer is partially crystallized with r-TiO_2 and a small fraction of Zn_2TiO_4, which embedded into the amorphous matrix (Fig. 2a-II1~II3). Moreover, Zn, Ti and O are also detected by EDX in the amorphous matrix of the sub-layer (inserted EDX spectrum). Given that Zn element contained in amorphous matrix of an as-MAOed layer presents in the form of Zn–O bond [26], it is clear that the contained Zn element in MAO_0 presents in two forms of Zn–O bond and Zn_2TiO_4, respectively.

After HT for 4 h, the surface of as-MAOed layer still appears porous in low magnification, while the high amplifying views reveal that the nanorods with a mean rod diameter of ~72 nm and an inter-rod spacing of ~81 nm hydrothermally grown on the surface of the layer (surface view in Fig. 2B). Based on the cross-sectional views and EDX profiles of Ti, O and Zn detected on the cross-sections (left image in Fig. 2B), together with XRD spectrum (Fig. S1, Supplementary data), it is revealed that the MAO and HT derived coating comprises a nanorods-arrayed outer layer composing of ZnO and showing a thickness of ~900 nm as well as a microporous inner layer adjacent to Ti substrate containing r-TiO_2 and Zn_2TiO_4, and the coating is consequently termed as ZNR. Notably, the roots of ZnO nanorods embed into the matrix of the inner layer to ensure a strong adhesion between the nanorods and their underlying layer. The bilayer structure of ZNR is further identified by the TEM images in Fig. 2B (right image). Based on the selected area electron diffraction (SAED) pattern (III-1), high resolution TEM image (HRTEM) (III-2) and the EDX (III-3) taken from III-marked micro-area in the panoramic TEM bright-field image, it is further confirmed that the nanorods in ZNR comprises ZnO single crystal, growing along the c-axis of the hexagonal crystal. Moreover, the bright-field image (IV-1), HRTEM images (IV-2 and 5), SAED pattern (IV-3) and dark-field image (IV-4) taken from IV-marked micro-area in the panoramic TEM bright-field image reveal that the inner layer underlying ZnO nanorods comprises an upper-layer of completely amorphism and a sub-layer with nanocrystalline TiO_2 and Zn_2TiO_4 to embed into the amorphous matrix. Although the hyperfine-structure of the inner layer of ZNR is similar with that of MAO_0, the Zn contents in both amorphism contained in the upper- and sub-layer are much less than those in the corresponding layers of MAO_0, as revealed by Fig. 2A–I3 showed and II1 inserted EDX spectra *vs.* Fig. 2B–IV6 depicted EDX spectra.

Current works have shown that ZnO arrays derived by HT always formed in the hydrothermal solution containing Zn^{2+}, which acts as the source of Zn to form ZnO [32,33], however, Zn-free hydrothermal solution was used to grow ZnO nanorods in situ on the as-MAOed layer in our present work. Thus, to identify the origination of Zn to form ZnO nanorods and investigate the growth process of these ZnO nanorods on the MAOed layer during HT, MAO_0 were hydrothermally treated (HTed) for 1 and 2 h, respectively, and the phase components of the resultant coatings were identified (Fig. S1, Supplementary data). Both the HTed coatings consist of r-TiO_2, Zn_2TiO_4 and ZnO, indicating the formation of ZnO during HT; moreover, with prolonging the duration of HT, the contents of ZnO in the coatings tend to increase. The surface and cross-sectional morphologies of the HTed coatings were also observed as shown in Fig. 3A. After HT for 1 h, ZnO nanogranules with a size of ~20 nm are observed to nucleate and grow on the MAOed layer. At 2 h of HT, these ZnO nanogranules grow longer and coarser, transitioning into nanorods with length of ~400 nm, diameter of ~72 nm and interrod spacing of ~81 nm. With prolonging the time to 4 h, these nanorods continually undergo significant growth in length, but exhibit almost no changes in diameter (Fig. 2B). Fig. 3B reveals the changes in depth profile of Zn element on the cross-section of the MAOed layer before and after HT for 2 and 4 h, respectively. The contents of Zn in the MAOed layer at the same distance from the ZnO nanorods/MAOed layer interfaces decreased with prolonging HT-duration time, revealing the Zn^{2+} incorporated in the MAOed layer migrating out to its surface during HT. Based on the fact of Zn decrease in the amorphism contained in the MAOed layer after HT (Fig. 2B *vs.* 2A) and much higher decomposition temperature of Zn_2TiO_4 than the HT temperature [34], it can be inferred that the migrated Zn^{2+} for nucleation and growth of ZnO nanorods derived from the Zn–O bonds contained in amorphous matrix rather than Zn_2TiO_4 contained in the MAOed layer. When the migrated Zn reaches supersaturation relative to ZnO on the surface of the MAOed layer, it reacted with hydroxyl groups in the hydrothermal solution to form ZnO nuclei [35] and grew in length into nanorods with prolonging HT time (Fig. 3A). The formation mechanism of ZnO nanorods during HT is schematically shown in Fig. 3C.

3.2. Evaluation of structural stability of ZNR

Strong bond strength between coatings and substrates can ensure a long-span service life of endosseous implants [36,37]. The bond strength of ZNR was examined using scratch test, as shown in Fig. 4A. The critical load (L_c) of the coating is 22.5 ± 1.4 N that causes initial delamination of ZNR (magnified I-marked area in Fig. 4A). As identified by the inserted EDX spectra, the delamination occurs in the interior of as-MAOed layer, rather than the interfaces of ZnO nanorods/MAOed layer or MAOed layer/Ti substrate. The results indicate that L_c characterizes the cohesive strengths of the coating and that the adhesive strengths between the coating and substrate as well as ZnO nanorods and as-MAOed layer are higher than the L_c. Notably, the L_c value of ZNR is far higher than the precipitation derived ZnO nanorod-like arrays on steel substrates [38]; moreover, the L_c value of ZNR is similar to that of HT derived TiO_2 nanorods-patterned coating on Ti (25.4 ± 0.9 N) that is not delamination even after 3.85×10^6 cycles at a cyclic load of 354.1 MPa [36]. Collectively, MAO and HT derived ZNR exhibits strong bond strength to ensure their long-life span in clinic.

The Zn^{2+} release profiles of M − Ti and ZNR-Ti in physiological saline (PS) are depicted in Fig. 4B, displaying that Zn^{2+} concentrations of the PS solution immersing M − Ti and ZNR-Ti tend to increase with immersion time. At each time point, M − Ti releases far more Zn^{2+} in amount than ZNR-Ti (Fig. 4B). Moreover, Zn^{2+} exhibits a burst release from ZNR-Ti within 24 h of immersion, resulting in higher Zn^{2+} concentration in the ZNR-Ti immersed PS compared to the minimum bactericidal concentration (MBC) of Zn^{2+}, which is 0.65 ppm [39,40]. Given the disorder nature of amorphism and almost insolubility of Zn_2TiO_4 [26], the released Zn^{2+} of M − Ti originates from the Zn–O bonds contained in the amorphous matrix of MAO_0. Regards to ZNR, besides of the Zn–O bonds contained in the amorphous matrix of the inner MAOed layer, Zn–O bonds contained in the ZnO nanorods are also the contributor for Zn^{2+} release of ZNR-Ti, due to the solubility of ZnO [41]. The results are identified by Fig. 4C and D, although no obvious change in morphology appearing in the immersed ZNR at low magnification (SEM image), the high amplifying view (TEM image) reveals the edge of the immersed ZnO nanorod is etched compared to that before immersion (Fig. 4D). However, the Zn–O bonds contained in amorphous

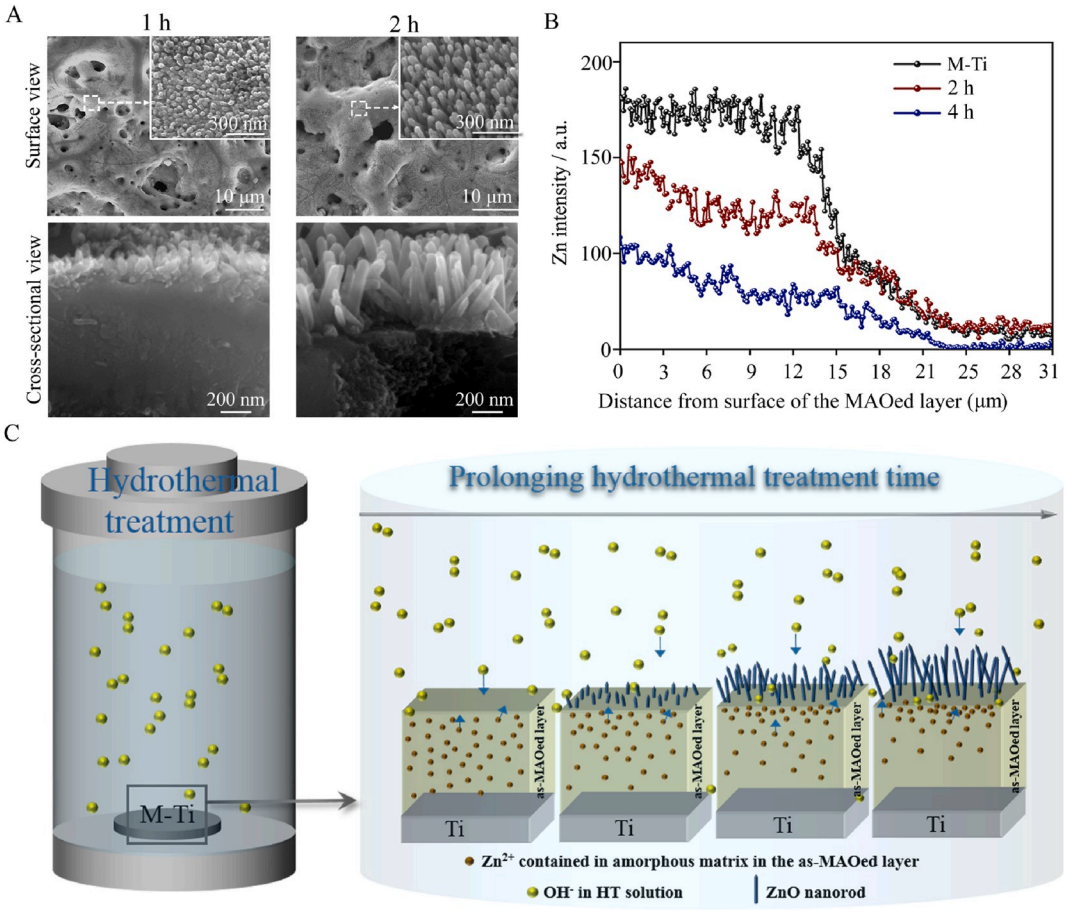

Fig. 3. (A) Surface and cross-sectional SEM morphologies of the 1 and 2 h HTed MAO_0; (B) in-depth distribution profiles of Zn in M − Ti, 2 h and 4 h HTed M-Ti; (C) schematic diagram showing the growth of ZnO nanorods during HT.

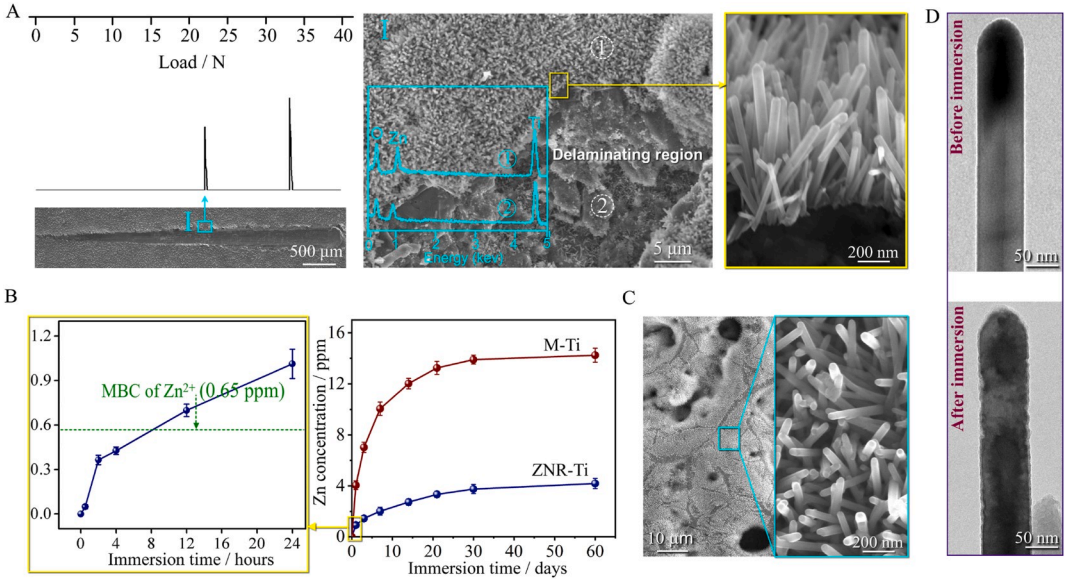

Fig. 4. (A) Bond strength of ZNR evaluated with scratch tests: curves of acoustic output versus load, scratch morphology, and the amplified view of the initial failure area caused by critical load (L_c) together with the inserted EDX spectrum detected on the ①-marked surface and ②-marked delaminating region of the coating; (B) Zn^{2+} concentrations of the PS solutions immersing M − Ti and ZNR-Ti discs as a function of immersion time (MBC: minimum bactericidal concentration); (C) surface morphology of ZNR after 60 days of immersion in PS solution; (D) TEM images of an individual ZnO nanorod before and after 60 days of immersion in PS solution.

matrix of the MAOed layer are thought to be relatively weaker than those in crystallized ZnO [26], together with the fact of Zn^{2+} migration out of MAOed layer to form ZnO nanorods during HT (Fig. 3B), it is easier to understand the lower release amount of Zn^{2+} from ZNR-Ti than M-Ti.

3.3. Antibacterial abilities of ZNR in vitro and in vivo

The release- and contact-killing manners of ZNR-Ti against Gram-positive bacteria, *S. aureus* and Gram-negative bacteria, *E. coli in vitro* and *in vivo* were tested, together with the control group of bare Ti without antibacterial activity [26]. The results are shown in Figs. 5 and S2 (Supplementary data), respectively.

As shown in Fig. 5A, the number of planktonic *S. aureus* colonies in the MHB immersing ZNR-Ti significantly decreases compared to that in the bare Ti immersed MHB, as assessed by counting bacterial colonies formed by picking up bacteria suspension immersing bare Ti and ZNR-Ti for 24 h and re-cultivating on agar. It is indicated the intense release-killing ability of ZNR.

Parallelly, the bactericidal effects of ZNR-Ti against the adhesive *S. aureus* after different incubation time were assessed by counting bacterial colonies (Fig. 5B), which formed by dissociating *S. aureus* from ZNR-Ti at each incubation time point and re-cultivating on agar. The bacterial colony number on ZNR-Ti significantly decreased compared to that on Ti within 5 min of incubation, and almost no viable bacteria are dissociated from ZNR-Ti after 24 h of incubation, while the bacteria cultured on bare Ti proliferate throughout the whole incubation period. Such bactericidal effect of ZNR-Ti is further identified by the live/dead staining images of *S. aureus* cultured on it, exhibiting significantly less viable bacteria (marked by green fluorescence) compared to those of bacteria cultured on bare Ti at each time point (Fig. 5C). The morphologies of *S. aureus* cultured on bare Ti and ZNR-Ti after different time were observed, as shown in Fig. 5D. The bacteria on bare Ti appear an intact ball-shaped morphology with smooth surface and the numbers increases with incubation time, keeping in line with the plate-counting and fluorescence-staining results (Fig. 5B and C). Moving to ZNR-Ti, after 5 min of incubation, extracellular polymeric substance (EPS) is secreted by *S. aureus* to adhere onto ZnO nanorods, moreover, EPS-induced adhesive force of bacteria to ZnO drove the nanorods to puncture bacterial cell wall (i.e., mechano-penetration, marked by red arrow in Fig. 5D). Due to the cell wall penetration induced distortion of the linkage between the bacterial outer membrane and peptidoglycan [42], the bacteria exhibits wrinkled surfaces. With prolonging incubation time, bacteria penetration becomes much deeper to induce severely damage of cell walls and plasma membranes, leading to the collapse of *S. aureus* and leakage of intracellular proteins, which is supported by the

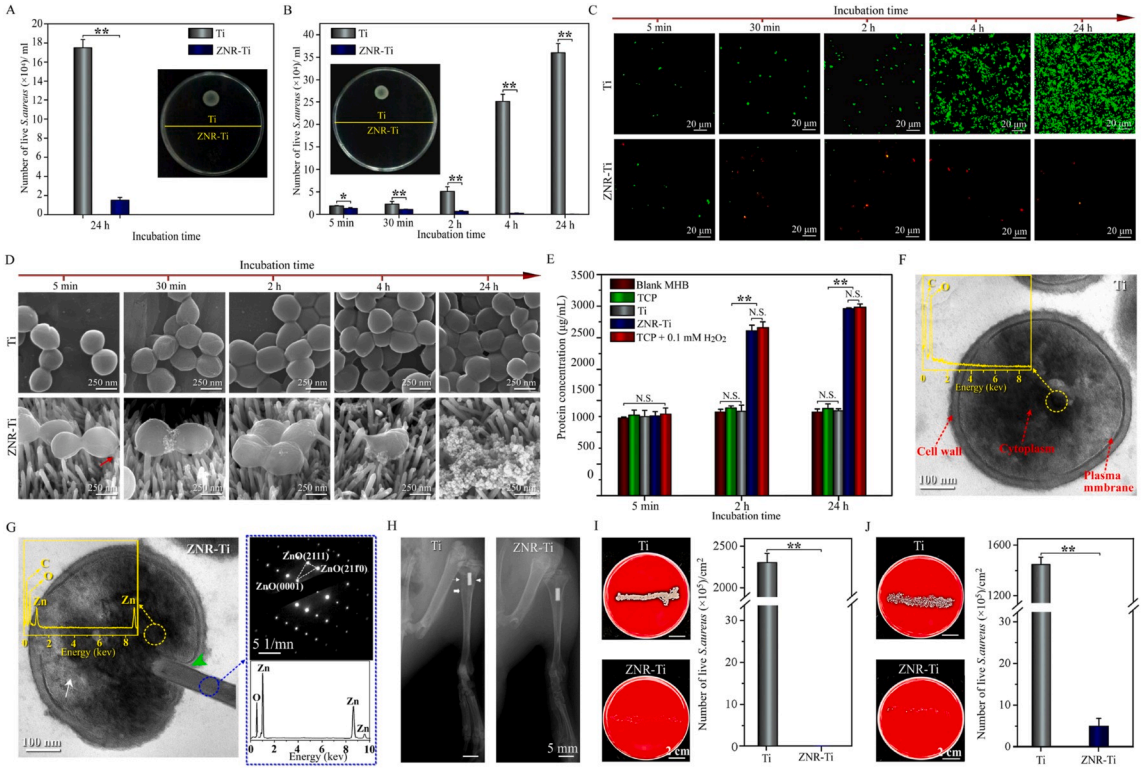

Fig. 5. The antibacterial activities of ZNR-Ti disc *in vitro* and *in vivo*. (A) Numbers of *S. aureus* colonies formed by picking up the bacteria suspensions from the MHB cultured with bare Ti and ZNR-Ti discs for 24 h and re-cultivating on agar for another 24 h, along with the inserted optical photograph of undiluted bacteria colonies formed by picking up *S. aureus* from the MHB immersing the bare Ti, ZNR-Ti discs and then re-cultivating on agar for 24 h; (B) numbers of undiluted bacteria colonies formed by dissociating *S. aureus* from the bare Ti and ZNR-Ti discs after different incubation time and then re-cultivating on agar for 24 h, along with the inserted optical photograph of undiluted bacteria colonies formed by dissociating *S. aureus* from the samples after 24 h of incubation and then re-cultivating on agar for 24 h; (C) fluorescent live/dead straining images and (D) SEM images of *S. aureus* cultured on the bare Ti and ZNR-Ti discs for different time; (E) protein concentrations of the MHB culturing *S. aureus* seeded on the bare Ti and ZNR-Ti discs for 5 min, 2 h and 24 h, together with the protein concentrations of blank MHB, the MHB culturing *S. aureus* seeded on tissue culture plate (TCP), and 0.1 mM H_2O_2 contained MHB culturing *S. aureus* seeded on TCP (namely TCP+0.1 mM H_2O_2) as controls; TEM images of *S. aureus* cultured on the (F) bare Ti and (G) ZNR-Ti discs for 2 h, together with the EDX spectra examined in the yellow dotted-circle marked areas in bacteria as well as the SAED pattern and EDX spectrum detected within the blue dotted-circle marked area of the nanorod; (H) laterally viewed X-ray images of *S. aureus*-infected tibias containing the bare Ti and ZNR-Ti pillars at 4 weeks of implantation (thin arrow showing an osteolysis-induced decrease in electron density and bold arrow showing an expansion of medullary cavity); photographs and the corresponding counted numbers of *S. aureus* colonies formed by rolling (I) the bare Ti and ZNR-Ti pillars implanted for 4 weeks together with (J) the peri-implant bone on blood agar plates and culturing for 24 h. All the data are expressed as means ± SD (n = 3). (*p < 0.05, **p < 0.01).

protein leakage assays (Fig. 5E). Eventually, the bacteria on ZNR-Ti are broke into debris at 24 h.

Progressively, to clarify the changes in morphologies of *S. aureus* cultured on the bare Ti and ZNR-Ti discs, the bacterial slices obtained from the bacteria cultured on bare Ti and ZNR-Ti for 2 h as representatives, were carefully observed by TEM (Fig. 5F and G). *S. aureus* cultured on the bare Ti disc displayed intact bacterial cell wall and plasma membrane as well as homogeneously distributed cytoplasm, containing C and O elements, as confirmed by EDX. Whereas, consistently with the SEM observation in Fig. 5D, the bacterial cell wall and plasma membrane are pierced by an individual ZnO nanorod (marked by green arrow and identified by SAED pattern and EDX profile detected in the blue dotted circle-marked area in Fig. 5G). Owing to the leakage of intracellular protein (Fig. 5E) through the punctured cell wall and plasma membrane, inhomogeneous distribution of cytoplasm is observed (white arrow). In addition, besides C and O, Zn element was also detected by EDX in the bacterial cytoplasm, revealing the influx of Zn^{2+} released from ZNR (Fig. 4B) into bacterial cytoplasm.

In addition, as shown in the plate-counting assessed bacterial colony numbers (Figs. S2a and b, Supplementary data), ZNR-Ti also exhibits bactericidal capability against the planktonic and the adhered *E.coli in vitro* with the respective bactericidal rates of 89.74% and 99.41%. Moreover, the live/dead staining were performed to examine the viable *E. coli* cultured on bare Ti and ZNR-Ti for 24 h and the results are shown in Fig. S2C. Intense green fluorescence is observed on bare Ti, indicating the large amount of live bacteria existing on Ti, while almost no viable bacteria exist on ZNR-Ti. The results are further confirmed by SEM images in Fig. S2D. Taken together, ZNR-Ti exhibits strong bactericidal activity against gram-negative *E. coli*, revealing a broad-spectrum bactericidal capability of ZNR.

The bactericidal capability of ZNR-Ti was also evaluated in *S. aureus*-infected rat bone marrow cavities. The ZNR-Ti pillars with the identical surface morphology to the disc-shaped ZNR-Ti (Fig. S3, Supplementary data) were implanted in *S. aureus*-infected rat tibia, together with the bare Ti pillars as a control group. Fig. 5H shows the lateral view X-ray images of the bare and coated Ti post 4 weeks of implantation. Expansion of the medullary cavity and osteolysis (marked by white arrows) are observed around the bare Ti pillar, suggesting the appearance of bacterial infection within bone due to the lack of antibacterial activity of bare Ti. However, in the case of the implanted ZNR-Ti pillar, bacteria infection induced osseous destruction is not observed within the peri-implant bone. Fig. 5I and J shows the photographs and the corresponding counted numbers of *S. aureus* colonies formed by rolling the bare Ti and ZNR-Ti pillars and the peri-implant bone separately after 4 weeks of implantation on blood agar plates and re-culturing for 24 h. *S. aureus* on the ZNR-Ti pillar and within the peri-implant bone exhibit a sharp reduce in amount compared to the respective ones corresponding to the bare Ti pillar, disclosing the still strong antibacterial activity of ZNR *in vivo*.

A great deal of works have been conducted to investigate the antibacterial capability of ZnO nanorod-like particles or coatings fabricated by various methods *in vitro* and *in vivo* [32,33,43–55]. To conveniently compare the antibacterial effects of our ZNR to that of ZnO contained nanoparticles or coatings mentioned in other works, their antibacterial rates together with bond strengths of ZnO coatings are summarized in Fig. 6. It is shown that ZnO nanorods-patterned coating fabricated in our work exhibit comparable or even higher antibacterial rate compared to ZnO nanorod-like particles [43,44] and coatings [32, 45–47,54,55] with [54,55] or without physical stimulation [32,45–47], other elements doped ZnO [33,48,49] and ZnO contained compounds [50–53], exhibiting the convenient usage of our coating in achieving high antibacterial efficacy. More crucially, our ZnO nanorods-patterned array is fabricated without using templates, catalysts and ZnO seeds, leading to that the bond strength of our ZNR is far higher compared to those of hydrothermal grown ZnO coating using ZnO seeds [38,56]. The aforementioned advantages of our MAO and HT derived ZnO nanorods-patterned array ensure its antibacterial performance in clinical application.

3.4. Quantitative evaluation of the contribution of mechano-penetration, formed ROS and released Zn^{2+} to the bactericidal activity of ZNR

Based on the aforementioned results, the bactericidal activity of ZNR is partially dependent on the mechano-penetration effect of ZnO nanorods against the adhered *S. aureus*. To identity whether ROS plays a role in the bactericidal activity of ZNR, the formation of ROS, including O_2^{-}·,

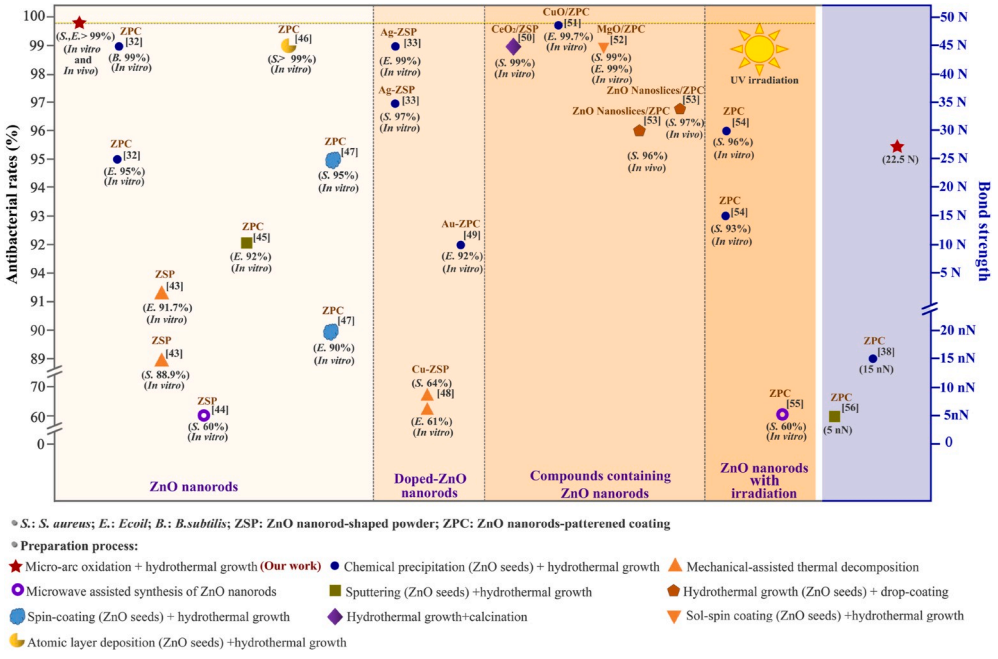

Fig. 6. Antibacterial rates of ZnO nanorod-like particles and coatings *in vitro* and *in vivo* as well as bond strengths of ZnO nanorods-patterned coatings mentioned in literatures and our ZNR.

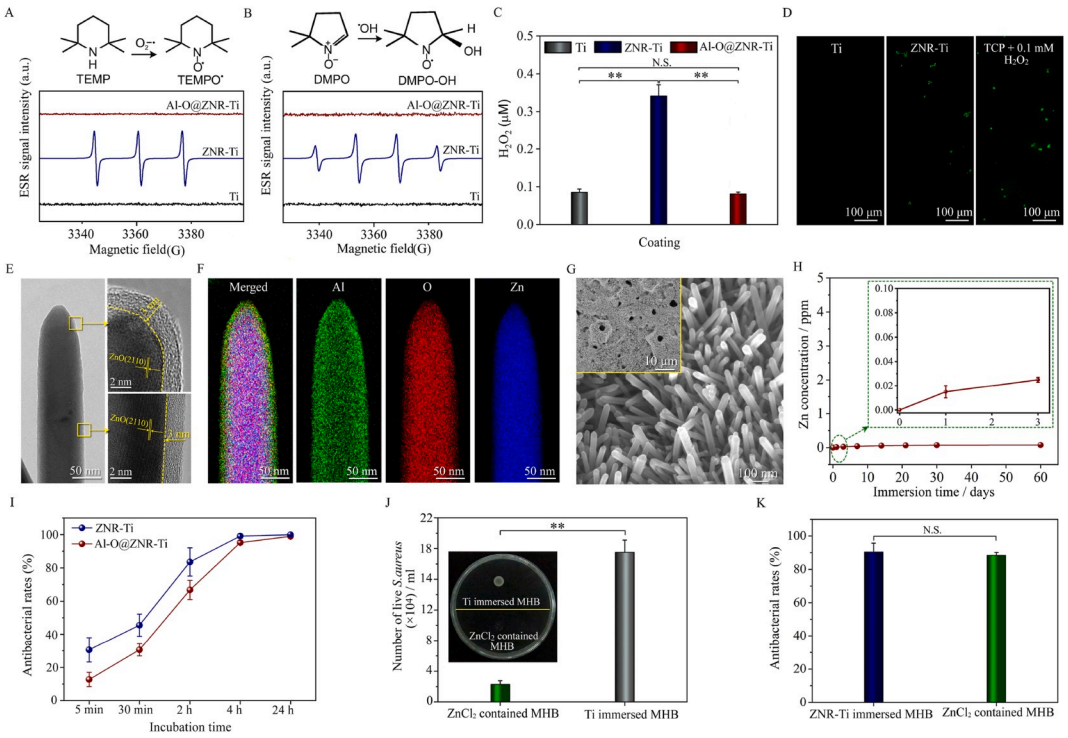

Fig. 7. The ESR spectra of (A) superoxide (O_2^{-}•) and (B) hydroxyl radical (•OH) in the MHB immersing the bare Ti, ZNR-Ti and Al–O@ZNR-Ti discs as detected using TEMPO· and DMPO-OH spin trap agents; (C) the concentrations of H_2O_2 in the MHB immersing the bare Ti, ZNR-Ti and Al–O@ZNR-Ti discs; (D) fluorescent straining images of ROS in *S. aureus* cultured on bare Ti, ZNR-Ti in MHB and on TCP in 0.1 mM H_2O_2 contained MHB; (E) TEM analyzed microstructures of Al–O@ZNR and (F) the distribution maps of Al, O, and Zn elements detected on the nanorod shown in (E) using TEM-equipped EDX; (G) surface SEM morphology of Al–O@ZNR; (H) Zn^{2+} concentration of the PS solution immersing Al–O@ZNR as a function of immersion time; (I) the reduction percentages of bacteria colony numbers on ZNR-Ti and Al–O@ZNR-Ti surfaces relative to that on the bare Ti after different incubation time (i. e. antibacterial rates); (J) numbers of undiluted bacteria colonies formed by picking up the 24 h-incubated planktonic *S. aureus* from the Ti immersed MHB and $ZnCl_2$ contained MHB and re-cultivating on agar for 24 h, along with the inserted optical photograph of these bacteria colonies; (K) the anti-bacterial rates against planktonic *S. aureus* of the $ZnCl_2$ contained MHB and ZNR-Ti immersed MHB after incubation for 24 h (*$p < 0.05$, **$p < 0.01$).

HO· and H_2O_2 in the ZNR-Ti disc immersed MHB was firstly performed using ESR spectroscopy (for O_2^{-}· and HO·) and H_2O_2 assay kits, respectively, together with the bare Ti disc immersed MHB as a negative control, as shown in Fig. 7A–C. No ESR adsorption peaks of O_2^{-}· and HO· are detected in the MHB immersing the bare Ti disc, and the concentration of H_2O_2 in bare Ti immersed MHB was comparable to that in the blank MHB tested in our previous work [26], revealing no ROS were formed on bare Ti in this medium. However, conspicuous O_2^{-}· and HO· species as well as H_2O_2 are formed on ZNR-Ti. It has been reported that ZnO synthesized at relatively low temperature exhibits surface defects (e.g., oxygen vacancy with one electron) [57], which reacts with O_2 to form O_2^{-}·. The formed O_2^{-}· can react with aqueous solution to induce hydroperoxyl radical that recombines to form H_2O_2, which reacts with O_2^{-}· to form HO· and hydroxyl ion [11]. Consequently, HT derived ZNR at 140 °C in the present work can induce ROS formation in MHB.

Subsequently, the intracellular ROS fluorescence staining tests were carried out for the bacteria cultured on the bare and coated Ti discs after 2 h of incubation, together with bacteria cultured in 0.1 mM H_2O_2 contained MHB on tissue culture plate (TCP) as a positive group. The obtained images are shown in Fig. 7D, in which the intracellular ROS level is characterized by green fluorescence intensity of the stained *S. aureus*. Although the intracellular ROS level of *S. aureus* cultured on ZNR-Ti is slightly lower than that of *S. aureus* cultured in 0.1 mM H_2O_2 contained MHB on TCP, it exhibits significant enhancement compared to that of *S. aureus* cultured on the bare Ti disc. For one hand, H_2O_2 formed on ZNR can enter bacteria efficiently and be transformed into HO· by ferrous ions through Fenton reaction [58] to elevate the intracellular ROS level; on the other hand, the released Zn^{2+} from ZNR can inflow into bacteria (Fig. 5G) through a zinc importer-ZnuABC with high affinity on cytoplasmic membrane [59], which could inactivate the cellular antioxidant pool and disrupt the metabolic balance to enhance intracellular ROS level *via* Fenton-like reactions [28,60,61].

Among the ZNR-derived extracellular ROS, HO· as the most reactive oxidant, together with O_2^{-}· ions oxidized and destroyed the peptidoglycan, the predominant component of bacterial cell wall, and the cytoplasmic membrane [62,63]. Furthermore, the flow of extracellular H_2O_2 and Zn^{2+} into cytoplasm derived intracellular ROS elevation not only aggravates the damage of phospholipid and thereby plasma membrane caused by the extracellular ROS, but also has additional harmful to intracellular proteins and DNA, ultimately accelerating bacteria death.

Based on the aforementioned results, it can be identified that the bactericidal activity of ZNR against the adhesive *S. aureus* is attributed to the synthetic effects of mechano-penetration of ZnO nanorods as well as ROS formation and Zn^{2+} release. To quantitatively clarify the contribution of each kind of these contributors, amorphous layer with a thickness of 3 nm (Fig. 7E) is deposited on each of the nanorods in ZNR using ALD, which contains Al and O elements, as identified by the elements maps in Fig. 7F, consequently the Al–O deposited ZNR is termed as Al–O@ZNR. Al–O@ZNR exhibits similar nanotopography to ZNR (Fig. 7G), while it does not release Zn^{2+} (Fig. 7H) and induce ROS formation (Fig. 7A–C), eliminating their contribution and preserving the sole contribution of mechano-penetration to bactericidal activity of ZNR. Based on the plate-counting assessed bacterial colony numbers (Fig. S4, Supplementary data), the bactericidal rates at each time point (i.e., the ratio of bacterial colony numbers on the coatings and bare Ti) of Al–O@ZNR and ZNR are shown in Fig. 7I. The bactericidal rates of ZNR and Al–O@ZNR are respective 30.6 ± 7.34% and 10.7 ± 3.27% at 5 min,

45.5 ± 6.72% and 27.6 ± 5.67% at 30 min, 83.6 ± 8.49% and 62.8 ± 6.77% at 2 h, 99.1 ± 1.26% and 96.2 ± 0.23% at 4 h, 99.9 ± 0.003% and 96.0 ± 1.01% at 24 h. Based on the facts of lower Zn^{2+} concentration released from ZNR than MBC within 4 h of incubation (Fig. 4B) and subsequently similar bactericidal rates of the two coatings (Fig. 7I), it is suggested that the predominant contributors against adhesive bacteria are mechano-penetration and ROS rather than released Zn^{2+}. Moreover, it also can be inferred from the results that the quantitative contribution of ROS to the bactericidal activity of ZNR against the adhesive bacteria is about 20%, which is the main contributor within 30 min of incubation. However, the contribution of mechano-penetration increases with time and eventually reached to ~96%, playing a predominant role in bactericidal activity of ZNR after 2 h of incubation. The transition of main contributors may ascribe to the no obviously variational surface defects in ZNR and the gradually increased adhesive force of the bacteria onto its underlying nanorods [64]. Collectively, for the adhered bacteria, ZNR induced ROS plays a key role in killing bacteria during the initial incubation period, appearing a contribution value of ~20%; while with prolonging incubation time, mechano-penetration of ZNR becomes the predominant contributor to its bactericidal activity with a high contribution value of ~96%, leading to the death of almost all the adhered bacteria. The bactericidal mechanism is illustrated in Fig. 8.

For killing the planktonic *S. aureus* in the MHB immersing ZNR-Ti, the effectors are the partially released ROS and Zn^{2+} from ZNR. To quantitatively clarify the contribution of released ROS and Zn^{2+} to kill the planktonic bacteria at 24 h of incubation, $ZnCl_2$ contained MHB is used to culture bacteria, which containing the same Zn^{2+} content with that of MHB immersing ZNR for 24 h (Fig. 4B). As shown in Fig. 7J and K, the bactericidal rate of $ZnCl_2$ contained MHB is 88.31% at 24 h, which is close to that of ZNR against planktonic *S. aureus* (Fig. 7K), indicating that the main contributor to kill the planktonic bacteria is the released Zn^{2+} from ZNR (Fig. 8).

4. Conclusions

A ZnO nanorods-patterned coating (ZNR) is fabricated on Ti by means of MAO and HT without using templates and catalysts at relatively low temperature. The coating comprises an outer layer of ZnO nanorods and an inner microporous MAOed layer composing of nanocrystalline TiO_2 and Zn_2TiO_4 to embed into Ti, O and Zn contained amorphous matrix. During HT, Zn^{2+} contained in the amorphous matrix of the MAOed layer rather than Zn_2TiO_4 migrates to the surface and reacts with OH^- in hydrothermal solution to form ZnO nucleation, which grew in length at expense of the migrated Zn^{2+}. The weak Zn–O bonds in amorphous matrix of the MAOed layer are identified to the predominantly contributor to the Zn^{2+} release of ZNR, which are expensed to form ZnO nanorods during HT, giving rise to the much lower Zn^{2+} release from ZNR than the as-MAOed coating (MAO_0) within the same immersion duration. ZNR exhibits intense bactericidal activity against the adhered and planktonic *S. aureus* and *E. coli in vitro* and *in vivo*. For the adhesive bacteria, the bactericidal contributors are the ZnO nanorods derived mechano-penetration and the ZnO induced ROS. It is revealed that ROS is the main contributor within 30 min of incubation with a steady quantitative contribution value of ~20%. However, owing to the gradually increased adhesive force of bacteria to its underlying nanorods, the predominant bactericidal contributor of ZNR transforms into mechano-penetration, and its contribution reached to 96% after 24 of incubation. For the planktonic bacteria, the bactericidal contributors are the released ROS and Zn^{2+} from ZNR, in which the released Zn^{2+} functions as the predominant contributor with the quantitative value of ~88.31% at 24 h of incubation.

CRediT authorship contribution statement

Jing Ye: Methodology, Investigation, Data curation, Visualization, Writing – original draft. **Bo Li:** Conceptualization, Methodology, Investigation, Data curation, Funding acquisition, Writing – review & editing. **Mei Li:** Data curation, Methodology. **Yufeng Zheng:** Supervision. **Shuilin Wu:** Supervision. **Yong Han:** Conceptualization, Funding acquisition, Supervision, Writing – review & editing.

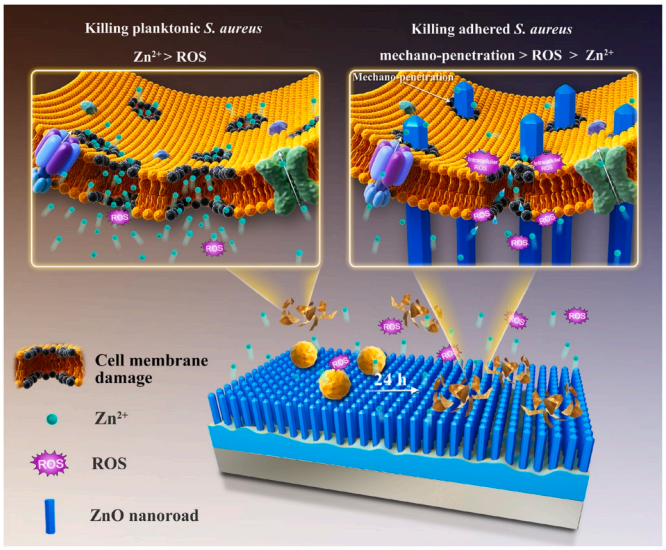

Fig. 8. Schematic illustration showing the antibacterial mechanism of ZNR against adhesive and planktonic *S. aureus*.

Declaration of competing interest

All authors declare that this original paper has not been submitted for publication in any other journal, confirming that the checked manuscript has been agreed to the submission. We also have approved the described research, if accepted, it will not be published elsewhere in the same form, in English or in any other language, without the written consent of the copyright-holder. Simultaneously, all the authors state no competing financial interest in this paper.

Acknowledgements

We appreciate the National Natural Science Foundation of China (Grant number 51631007, 51971171 and 31700860) for financially supporting this work.

Appendix A. Supplementary data

Supplementary data to this article can be found online at https://doi.org/10.1016/j.bioactmat.2021.09.019.

References

[1] Z. Zhao, R. Yan, X. Yi, J. Li, J. Rao, Z. Guo, Y. Yang, W. Li, Y.-Q. Li, C. Chen, Bacteria-activated theranostic nanoprobes against methicillin-resistant *staphylococcus aureus* infection, ACS Nano 11 (2017) 4428–4438.
[2] K.G. Neoh, X. Hu, D. Zheng, E.T. Kang, Balancing osteoblast functions and bacterial adhesion on functionalized titanium surfaces, Biomaterials 33 (2012) 2813–2822.
[3] P. Li, Y.F. Poon, W. Li, H.-Y. Zhu, S.H. Yeap, Y. Cao, X. Qi, C. Zhou, M. Lamrani, R. W. Beuerman, Y.M. En-Tang Kang, C.M. Li, M.W. Chang, S.S.J. Leong, M.B. Chan-Park, A polycationic antimicrobial and biocompatible hydrogel with microbe membrane suctioning ? ability, Nat. Mater.
[4] H. Chouirfa, H. Bouloussa, V. Migonney, C. Falentindaudre, Review of titanium surface modification techniques and coatings for antibacterial applications, Acta Biomater. 83 (2019) 37–54.
[5] M. Rizwan, R. Alias, U.Z. Zaidi, R. Mahmoodian, M. Hamdi, Surface modification of valve metals using plasma electrolytic oxidation for antibacterial applications: a review, J. Biomed. Mater. Res. 106 (2018) 590–605.
[6] F. Zhang, B. Wang, Y. Shen, Blue luminescent ZnO nanoclusters stabilized by esterifiable polyamidoamine dendrimers and their UV-shielding applications, Asian J. Chem. 26 (2014) 3467–3470.

[7] Y. Zeng, X. Chen, Z. Yi, Y. Yi, X. Xu, Fabrication of p-n heterostructure ZnO/Si moth-eye structures: antireflection, enhanced charge separation and photocatalytic properties, Appl. Surf. Sci. 441 (2018) 40–48.

[8] Z. Han, Y. Li, X. Lin, Z. Wang, Z. Li, H. Wang, Preparation and photoelectrocatalytic performance of Fe_2O_3/ZnO composite electrode loading on conductive glass, Chem. J. Chin. Univ. 4 (2020) 308–316.

[9] Z. Han, Y. Li, F. Chen, S. Tang, P. Wang, Preparation of ZnO/Ag_2O nanofibers by coaxial electrospinning and study of their photocatalytic properties, Chem. J. Chin. Univ. 4 (2018) 771–778.

[10] Y. Liang, M. Wang, Z. Zhang, G. Ren, Y. Liu, S. Wu, J. Shen, Facile synthesis of ZnO QDs@GO-CS hydrogel for synergetic antibacterial applications and enhanced wound healing, Chem. Eng. J. 378 (2019) 122043.

[11] V. Lakshmi Prasanna, R. Vijayaraghavan, Insight into the mechanism of antibacterial activity of ZnO: surface defects mediated reactive oxygen species even in the dark, Langmuir 31 (2015) 9155–9162.

[12] N. Talebian, S.M. Amininezhad, M. Doudi, Controllable synthesis of ZnO nanoparticles and their morphology-dependent antibacterial and optical properties, J. Photochem. Photobiol., B 120 (2013) 66–73.

[13] S. Fanny Chiat Orou, K.J. Hang, M. Thuya Thien, Y.L. Ying, L.C. Foh, N. Duong Ngoc Diem, B.H. Goh, S.Y. Pung, Y.F. Pung, Antibacterial activity by ZnO nanorods and ZnO nanodisks: a model used to illustrate "Nanotoxicity Threshold", J. Ind. Eng. Chem. 62 (2018) 333–340.

[14] Y. Sun, G.M. Fuge, M.N.R. Ashfold, Growth of aligned ZnO nanorod arrays by catalyst-free pulsed laser deposition methods, Chem. Phys. Lett. 396 (2004) 21–26.

[15] H. Yuan, Y. Zhang, Preparation of well-aligned ZnO whiskers on glass substrate by atmospheric MOCVD, J. Cryst. Growth 263 (2004) 119–124.

[16] T. Nobis, E.M. Kaidashev, A. Rahm, M. Lorenz, J. Lenzner, M. Grundmann, Spatially inhomogeneous impurity distribution in ZnO micropillars, Nano Lett. 4 (2004) 797–800.

[17] R. Shi, P. Yang, X. Dong, Q. Ma, A. Zhang, Growth of flower-like ZnO on ZnO nanorod arrays created on zinc substrate through low-temperature hydrothermal synthesis, Appl. Surf. Sci. 264 (2013) 162–170.

[18] J. Lee, B.S. Kang, B. Hicks, T.F. Chancellor, B.H. Chu, H.-T. Wang, B.G. Keselowsky, F. Ren, T.P. Lele, The control of cell adhesion and viability by zinc oxide nanorods, Biomaterials 29 (2008) 3743–3749.

[19] R. Zhang, X. Liu, Z. Xiong, Q. Huang, X. Yang, H. Yan, J. Ma, Q. Feng, Z. Shen, Novel micro/nanostructured TiO_2/ZnO coating with antibacterial capacity and cytocompatibility, Ceram. Int. 44 (2018) 9711–9719.

[20] B. Li, Y. Han, K. Qi, Formation mechanism, degradation behavior, and cytocompatibility of a nanorod-shaped ha and pore-sealed MgO bilayer coating on magnesium, ACS Appl. Mater. Interfaces 6 (2014) 18258–18274.

[21] B. Li, P. Gao, H. Zhang, Z. Guo, Y. Zheng, Y. Han, Osteoimmunomodulation, osseointegration, and in vivo mechanical integrity of pure Mg coated with HA nanorod/pore-sealed MgO bilayer, Biomater. Sci. 6 (2018) 3202–3218.

[22] J. Zhou, B. Li, L. Zhao, L. Zhang, Y. Han, F-doped micropore/nanorod hierarchically patterned coatings for improving antibacterial and osteogenic activities of bone implants in bacteria-infected cases, ACS Biomater. Sci. Eng. 3 (2017) 1437–1450.

[23] K.S. Lee, C.H. Kim, S.W. Jeong, Y. Song, N.H. Bae, S.J. Lee, K.G. Lee, Ultrasonic fabrication of flexible antibacterial ZnO nanopillar array film, Colloids Surf. B Biointerfaces 170 (2018) 172–178.

[24] Q. Luo, H. Cao, L. Wang, X. Ma, X. Liu, ZnO@ZnS nanorod-array coated titanium: good to fibroblasts but bad to bacteria, J. Colloid Interface Sci. 579 (2020) 50–60.

[25] P.L. Bhutiya, M.S. Mahajan, M. Abdul Rasheed, M. Pandey, S. Zaheer Hasan, N. Misra, Zinc oxide nanorod clusters deposited seaweed cellulose sheet for antimicrobial activity, Int. J. Biol. Macromol. 112 (2018) 1264–1271.

[26] J. Ye, B. Li, M. Li, Y. Zheng, S. Wu, Y. Han, ROS induced bactericidal activity of amorphous Zn-doped titanium oxide coatings and enhanced osseointegration in bacteria-infected rat tibias, Acta Biomater. 107 (2020) 313–324.

[27] S. Jiang, K. Lin, M. Cai, ZnO nanomaterials: current advancements in antibacterial mechanisms and applications, Front. Chem. 8 (2020), 580-580.

[28] M.I. Setyawati, C.Y. Tay, D.T. Leong, Effect of zinc oxide nanomaterials-induced oxidative stress on the p53 pathway, Biomaterials 34 (2013) 10133–10142.

[29] G.W. Han, I.P. Jones, R.E. Smallman, Direct evidence for Suzuki segregation and Cottrell pinning in MP159 superalloy obtained by FEG(S)TEM/EDX, Acta Mater. 51 (2003) 2731–2742.

[30] Q. Chang, H. He, J. Zhao, M. Yang, J. Qu, Bactericidal activity of a Ce-promoted Ag/$ALPO_4$ catalyst using molecular oxygen in water, Environ. Sci. Technol. 42 (2008) 1699–1704.

[31] L. Zhao, H. Wang, K. Huo, L. Cui, W. Zhang, H. Ni, Y. Zhang, Z. Wu, P.K. Chu, Antibacterial nano-structured titania coating incorporated with silver nanoparticles, Biomaterials 32 (2011).

[32] T.O. Okyay, R.K. Bala, H.N. Nguyen, R. Atalay, Y. Bayam, D.F. Rodrigues, Antibacterial properties and mechanisms of toxicity of sonochemically grown ZnO nanorods, RSC Adv. 5 (2015) 2568.

[33] T. Jan, J. Iqbal, M. Ismail, A. Mahmood, Synthesis of highly efficient antibacterial agent Ag doped ZnO nanorods: structural, Raman and optical properties, J. Appl. Phys. 115 (2014) 154308.

[34] D. Sun, X. Yan, J. Chen, S. Yu, L. Hu, Q. Xue, Fabrication of Zn_2TiO_4 and TiN nanofibers by pyrolysis of electrospun precursor fibers, CrystEngComm 13 (2011) 3905–3909.

[35] Z.L. Wang, ZnO nanowire and nanobelt platform for nanotechnology, Mater. Sci. Eng. R 64 (2009) 33–71.

[36] H.W. Yang, M. Yu, R. Wang, B. Li, X. Zhao, Y.L. Hao, Z. Guo, Y. Han, Hydrothermally grown TiO_2-nanorods on surface mechanical attrition treated Ti: improved corrosion fatigue and osteogenesis, Acta Biomater. 116 (2020) 400–414.

[37] D. Yu, S. Guo, D. Yang, B. Li, Z. Guo, Y. Han, Interrod spacing dependent angiogenesis and osseointegration of Na_2TiO_3 nanorods-patterned arrays *via* immunoregulation, Chem. Eng. J. 426 (2021) 131187.

[38] G.J. Ehlert, U. Galan, H.A. Sodano, Role of surface chemistry in adhesion between ZnO nanowires and carbon fibers in hybrid composites, ACS Appl. Mater. Interfaces 5 (2013) 635–645.

[39] X. Wang, S. Liu, M. Li, P. Yu, X. Chu, L. Li, G. Tan, Y. Wang, X. Chen, Y. Zhang, C. Ning, The synergistic antibacterial activity and mechanism of multicomponent metal ions-containing aqueous solutions against *Staphylococcus aureus*, J. Inorg. Biochem. 163 (2016) 214–220.

[40] K.M. Reddy, K. Feris, J. Bell, D.G. Wingett, C. Hanley, A. Punnoose, Selective toxicity of zinc oxide nanoparticles to prokaryotic and eukaryotic systems, Appl. Phys. Lett. 90 (2007).

[41] J. Sawai, Quantitative evaluation of antibacterial activities of metallic oxide powders (ZnO, MgO and CaO) by conductimetric assay, J. Microbiol. Methods 54 (2003) 177–182.

[42] D. Greif, D. Wesner, J. Regtmeier, D. Anselmetti, High resolution imaging of surface patterns of single bacterial cells, Ultramicroscopy 110 (2010) 1290–1296.

[43] R. Sharma, M. Khanuja, S.S. Islam, U. Singhal, A. Varma, Aspect-ratio-dependent photoinduced antimicrobial and photocatalytic organic pollutant degradation efficiency of ZnO nanorods, Res. Chem. Intermed. 43 (2017) 5345–5364.

[44] P. Sadhukhana, M. Kundua, S. Ranab, R. Kumarb, J. Dasb, P.C. Sila, Microwave induced synthesis of ZnO nanorods and their efficacy as a drug carrier with profound anticancer and antibacterial properties, Toxicology Reports 6 (2019) 176–185.

[45] E. Jeong, C.U. Kimc, J. Byuna, J. Lee, H.-E. Kima, E.-J. Kim, K.J. Choi, S. Hong, Quantitative evaluation of the antibacterial factors of ZnO nanorod arrays under dark conditions: physical and chemical effects on *Escherichia coli* inactivation, Sci. Total Environ. 712 (2020) 136574.

[46] Z. Zhong, Z. Xu, T. Sheng, J. Yao, W. Xing, Y. Wang, Unusual air filters with ultrahigh efficiency and antibacterial functionality enabled by ZnO nanorods, ACS Appl. Mater. Interfaces 7 (2015) 21538–21544.

[47] Y. Xiang, J. Li, X. Liu, Z. Cui, X. Yang, K.W.K. Yeung, H. Pan, S. Wu, Construction of poly(lactic-co-glycolic acid)/ZnO nanorods/Ag nanoparticles hybrid coating on Ti implants for enhanced antibacterial activity and biocompatibility, Mater. Sci. Eng. C 79 (2017) 629–637.

[48] T. Bhuyan, M. Khanuja, R. Sharma, S. Patel, M.R. Reddy, S. Anand, A. Varma, A comparative study of pure and copper (Cu)-doped ZnO nanorods for antibacterial and photocatalytic applications with their mechanism of action, J. Nano Res. 17 (2015) 288.

[49] K. Sornsanit, M. Horprathumb, P. Eiamchaic, C. Chananonnawathornd, S. Kalasunge, J. Kaewkhaof, Enhanced antibacterial activity by Au nanoparticle decorated ZnO nanorods, Key Eng. Mater. 675 (2016) 113–116.

[50] S. Lan, X. Sheng, Y. Lu, C. Li, S. Zhao, N. Liu, Modification of antibacterial ZnO nanorods with CeO_2 nanoparticles: role of CeO_2 in impacting morphology and antibacterial activity, Colloid Interface Sci. 26 (2018) 32–38.

[51] R. Gandotraa, Y.-R. Chena, T. Murugesana, T.-W. Changa, H.-Y. Changc, H.-N. Lina, Highly efficient and morphology dependent antibacterial activities of photocatalytic Cu_xO/ZnO nanocomposites, J. Alloys Compd. 873 (2021) 159769.

[52] M. Du, M. Peng, B. Mai, F. Hu, X. Zhang, Y. Chen, C. Wang, A multifunctional hybrid inorganic-organic coating fabricated on magnesium alloy surface with antiplatelet adhesion and antibacterial Activities, Surf. Coating. Technol. 384 (2020) 125336.

[53] H. Liao, X. Miao, J. Ye, T. Wu, Z. Deng, C. Li, J. Jia, X. Cheng, X. Wang, Falling Leaves inspired ZnO nanorods−nanoslices hierarchical structure for implant surface modification with two stage releasingfeatures, ACS Appl. Mater. Interfaces 9 (2017) 13009–13015.

[54] M.H. Al-Hinai, P. Sathe, M.Z. Al-Abri, S. Dobretsov, A.T. Al-Hinai, J. Dutta, Antimicrobial activity enhancement of poly(ether sulfone) membranes by in situ growth of ZnO nanorods, ACS Omega 2 (2017) 3157–3167.

[55] F. Achouri, C. Merlin, S. Corbel, H. Alem, L. Mathieu, L. Balan, G. Medjahdi, M. B. Said, A. Ghrabi, R. Schneider, ZnO Nanorods with high photocatalytic and antibacterial activity under solar light irradiation, Materials 11 (2018) 2158.

[56] J.-E. Lee, H.-J. Kim, D.-E. Kim, Assessment of adhesion between thin film and silicon based on a scratch test, J. Mech. Sci. Technol. 24 (2010) 97–101.

[57] R. Sharma, M. Khanuja, S.S. Islam, U. Singhal, A. Varma, Aspect-ratio-dependent photoinduced antimicrobial and photocatalytic organic pollutant degradation efficiency of ZnO nanorods, Res. Chem. Intermed. 43 (2017) 5345–5364.

[58] M. Wang, Z. Hou, A.A.A. Kheraif, B. Xing, J. Lin, Mini review of TiO_2-based multifunctional nanocomposites for near-infrared light-responsive phototherapy, Adv. Healthc. Mater. 7 (2018) 1800351.

[59] M. Cerasi, S. Ammendola, A. Battistoni, Competition for zinc binding in the host-pathogen interaction, Front. Cell Infect. Microbiol. 3 (2013), 108-108.

[60] S.J. Stohs, D. Bagchi, Oxidative mechanisms in the toxicity of metal ions, Free Radical Bio, Med. Times 18 (1995) 321–336.

[61] C.C. Otto, J.L. Koehl, D. Solanky, S.E. Haydel, Metal ions, not metal-catalyzed oxidative stress, cause clay leachate antibacterial activity, PloS One 9 (2014), e115172.

[62] S. Noimark, C.W. Dunnill, I.P. Parkin, Shining light on materials-A self-sterilising revolution, Adv. Drug Deliv. Rev. 65 (2013) 570–580.

[63] Y. Takatsuji, S. Ishikawa, T. Haruyama, Efficient sterilization using reactive oxygen species generated by a radical vapor reactor, Process Biochem. 54 (2017) 140–143.

[64] C. Berne, C.K. Ellison, A. Ducret, Y.V. Brun, Bacterial adhesion at the single-cell level, Nat. Rev. Microbiol. 16 (2018) 616–627.